Chemical Science

EDGE ARTICLE

View Article Online
View Journal | View Issue

Cite this: *Chem. Sci.*, 2018, **9**, 8946

All publication charges for this article have been paid for by the Royal Society of Chemistry

Received 19th July 2018
Accepted 30th September 2018

DOI: 10.1039/c8sc03209b

rsc.li/chemical-science

Enhanced annihilation electrochemiluminescence by nanofluidic confinement†

Hanan Al-Kutubi,‡[a] Silvia Voci,‡[b] Liza Rassaei,[cd] Neso Sojic *[b] and Klaus Mathwig *[a]

Microfabricated nanofluidic electrochemical devices offer a highly controlled nanochannel geometry; they confine the volume of chemical reactions to the nanoscale and enable greatly amplified electrochemical detection. Here, the generation of stable light emission by electrochemiluminescence (ECL) in transparent nanofluidic devices is demonstrated for the first time by exploiting nanogap amplification. Through continuous oxidation and reduction of $[Ru(bpy)_3]^{2+}$ luminophores at electrodes positioned at opposite walls of a 100 nm nanochannel, we compare classic redox cycling and ECL annihilation. Enhanced ECL light emission of attomole luminophore quantities is evidenced under ambient conditions due to the spatial confinement in a 10 femtoliter volume, resulting in a short diffusion timescale and highly efficient ECL reaction pathways at the nanoscale.

Introduction

Electrochemiluminescence (ECL) is the emission of light by electrochemical means: reactive species are generated at the electrode surface and undergo a highly exergonic electron-transfer reaction producing the excited state of the luminophore.[1] It relaxes to the ground state, emitting a photon. The possibility to regenerate the reactive species *in situ* as well as not requiring an external light source for excitation, gives this method many advantages for (bio)sensing applications, single object imaging,[2–4] and light-emitting devices.[5] These advantages include a straightforward experimental setup, a very high sensitivity and a wide detection range. Thus, applications and fundamental aspects of ECL have been researched extensively.[5]

Whereas the precise mechanism of light generation depends on the species involved, there are two dominant pathways: the annihilation and the co-reactant pathways.[1] Here, we focus on the annihilation pathway in a nanochannel, in which light is generated through a reaction between the oxidized and reduced forms of the original compound. We selected tris(bipyridine) ruthenium(II), $[Ru(bpy)_3]^{2+}$, one of the most well-studied ECL compounds[6,7] due to its relatively high quantum yield, water solubility and long-lived triplet excited state. Its annihilation pathway is:[8]

$$[Ru(bpy)_3]^{2+} + e^- \rightarrow [Ru(bpy)_3]^{+} \quad (1)$$

$$[Ru(bpy)_3]^{2+} - e^- \rightarrow [Ru(bpy)_3]^{3+} \quad (2)$$

$$[Ru(bpy)_3]^{+} + [Ru(bpy)_3]^{3+} \rightarrow [Ru(bpy)_3]^{2+} + [Ru(bpy)_3]^{2+}* \quad (3)$$

$$[Ru(bpy)_3]^{2+}* \rightarrow [Ru(bpy)_3]^{2+} + h\nu. \quad (4)$$

These reactions were initially investigated by rapidly pulsing a single electrode between the oxidizing and reducing potential.[9,10] However, this technique suffers from drawbacks[11] such as large charging currents. Using two electrodes, both $[Ru(bpy)_3]^{+}$ and $[Ru(bpy)_3]^{3+}$ can be generated in close vicinity under steady-state conditions. Various two-electrode setups have been employed, including ring and disk electrodes,[12] thin layer cells,[13] band electrodes,[14–16] and scanning electrochemical microscopy.[17,18] These studies have shown that annihilation occurs more efficiently at smaller inter-electrode distances[16,18] as the diffusional distance between electrogenerated $[Ru(bpy)_3]^{+}$ and $[Ru(bpy)_3]^{3+}$ is decreased. Indeed, the stability of the reduced form, $[Ru(bpy)_3]^{+}$, is a key issue limiting the efficiency of the annihilation ECL. Yet, observation of light emission so far has been limited to a minimum inter-electrode distance of 2 μm.[18,19] In addition, due to the sensitivity of annihilation ECL towards impurities such as dioxygen and water, experiments are performed in drastic conditions: dried and distilled solvents just before use, recrystallized and dried luminescent compounds and supporting electrolytes, under an inert

[a]University of Groningen, Groningen Research Institute of Pharmacy, Pharmaceutical Analysis, P.O. Box 196, 9700 AD Groningen, The Netherlands. E-mail: kmathwig@rug.nl

[b]University of Bordeaux, Bordeaux INP, Institut des Sciences Moléculaires, UMR CNRS 5255, 33607 Pessac, France. E-mail: neso.sojic@enscbp.fr

[c]Rotterdam School of Management, Erasmus University, Burgemeester Oudlaan 50, 3062 PA Rotterdam, The Netherlands

[d]Delft University of Technology, Van der Maasweg 9, 2629 HZ Delft, The Netherlands

† Electronic supplementary information (ESI) available: Chemical reagents, device fabrication, background measurement, and finite element modeling, numerical concentration profiles. See DOI: 10.1039/c8sc03209b

‡ These authors contributed equally.

atmosphere or in a dry box.[15,18,20] This is especially true for platinum electrodes as the reduction potential for water/dioxygen competes with that of $[Ru(bpy)_3]^{2+}$.

Here, ECL emission is observed under ambient conditions using platinum electrodes in electrochemical nanogap devices.[21] We exploit the spatial confinement of such devices to enhance the annihilation ECL-reaction of $[Ru(bpy)_3]^{2+}$ and to reduce the effects of impurities. Microfabrication allows precise control of a nanofluidic channel geometry; two individually addressable electrodes positioned at the top and bottom of a nanochannel are separated by a distance of 100 nm or less (see Fig. 1).

The nanoscale distance between electrodes results in short diffusion times between them and gives rise to highly amplified currents through electrochemical redox cycling. Reversibly electrochemically active analytes are repeatedly oxidized and reduced as they diffuse between both electrodes, shuttling electrons across the nanochannel. At diffusion times of ~10 μs, each analyte molecule contributes thousands of electrons per seconds to the detected limiting current, which, thus, is highly amplified. Due to efficient redox cycling and a confined geometry, nanogap transducers and similar geometries have been employed for, *e.g.*, studying adsorption,[22] migration,[23,24] biosensing,[25] single-molecule electrochemistry,[26] and spectroelectrochemistry.[27]

Herein, for the first time, annihilation ECL is examined in transparent nanofluidic electrochemical devices. We report enhanced light emission due to highly efficient reaction pathways at the nanoscale. Light emission is stable at ambient conditions due to reduced degradation by contaminants.

Results and discussion

Nanogap devices were fabricated as described previously,[28,29] except that a transparent glass substrate was used. Due to the transparency and lower heat conductivity of glass, most fabrication steps had to be altered completely. In brief, structures comprising a thin 20 nm Pt bottom electrode, 100 nm Cr sacrificial layer (forming the nanochannel volume) and 120 nm Pt top electrode were patterned on a 10 cm borosilicate glass wafer using UV lithography followed by evaporation deposition and lift-off. A 500 nm SiO_2/SiN passivation layer, deposited using chemical vapor deposition, encased the devices. Access holes were etched through the passivation layer by reactive ion etching. Finally, the wafer was diced into individual chips. Before experimentation, a polydimethylsiloxane fluid reservoir was placed on top of the device, and the sacrificial Cr layer was selectively wet-etched to form the channel. In Fig. 1a, a device is shown with a 5 μm × 32 μm × 100 nm channel volume, and an effective area of overlap between the electrodes of 3 μm × 20 μm.

Electrochemical measurements were performed with a bipotentiostat (Autolab – PGSTAT30). Functioning simultaneously as both reference electrode and counter electrode, we used an Ag/AgCl/KCl (3 M) electrode in water, or an Ag wire in acetonitrile, respectively. For all experiments, freshly etched devices were cleaned by cycling the potential of both electrodes between −0.15 V and 1.2 V *vs.* Ag/AgCl in 50 mM H_2SO_4. Channels were thoroughly flushed with Milli-Q water, and subsequently with acetonitrile, which was then replaced by 10 mM $Ru(bpy)_3(PF_6)_2$ and 0.1 M $TBAPF_6$ in acetonitrile. This solution was used for all experiments.

We investigated two electrochemical 'modes' in the nanofluidic channel (see Fig. 2). In redox cycling, the top electrode is biased at an oxidizing potential generating $[Ru(bpy)_3]^{3+}$. Biasing the bottom electrode at 0 V leads to the one-electron reduction of $[Ru(bpy)_3]^{3+}$ and, thus, regeneration of $[Ru(bpy)_3]^{2+}$. In annihilation ECL, the same potential is imposed at the top electrode whereas the bottom electrode is placed at a sufficiently cathodic potential to reduce $[Ru(bpy)_3]^{2+}$ to $[Ru(bpy)_3]^{+}$. The annihilation reaction (3) takes place, and ECL light is emitted (4). Conceptually, this process is similar to redox cycling as it involves the constant consumption and regeneration of $[Ru(bpy)_3]^{2+}$. However, instead of taking place between the two electrode surfaces, regeneration (annihilation) occurs homogeneously in the channel bulk, where $[Ru(bpy)_3]^{+}$ and $[Ru(bpy)_3]^{3+}$ meet. In the top region, redox cycling between $[Ru(bpy)_3]^{2+}$ and its oxidized form occurs, whereas the bottom region shows cycling of $[Ru(bpy)_3]^{2+}$ with the reduced form. The channel is therefore effectively split, and anodic and cathodic redox cycling occur simultaneously (Fig. 2b). Therefore, as diffusion times scale inversely with the length of the diffusive path, switching from redox cycling to annihilation ECL mode should result in a higher faradaic current.

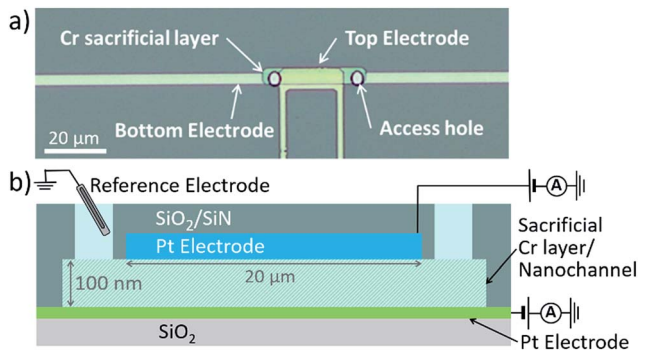

Fig. 1 (a) Top view optical micrograph of an electrochemical nanogap device. (b) Schematic cross section of a device with access holes to reservoir and two individually addressable Pt electrodes. The sacrificial Cr layer is etched before the experiments to form the nanochannel.

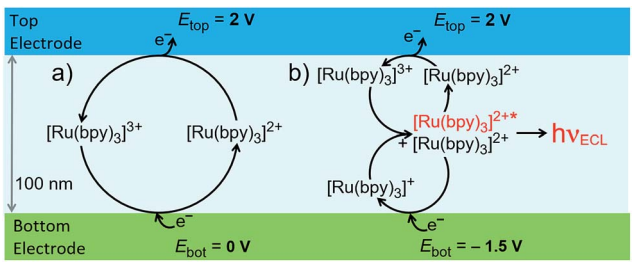

Fig. 2 Schematic of two reaction pathways in the nanochannel: (a) redox cycling, and (b) annihilation leading to ECL emission.

ECL-emission is produced in annihilation mode inside a nanochannel and was imaged and spatially resolved as shown in Fig. 3 using an epifluorescence microscope (DMI6000, Leica). Photon emission was collected by an inverted 40× microscope objective and detected by an Electron Multiplying Charge Coupled Device (EM-CCD) Camera (Hamamatsu, 9100-13). Light emission from a luminophore quantity of 60 attomoles present in the active area of the device was intense enough to be recorded through the 20 nm-thick semi-transparent Pt bottom electrode, due to nanogap amplification. The overlay image (Fig. 3a, right) shows that ECL intensity is uniform along the channel and decreases rapidly at the edges. No emission is seen from the bottom electrode area under the access holes. Furthermore, ECL emission is limited to a region narrower than the 5 μm wide channel. This indicates that emission is caused exclusively by reaction in the 3 μm × 20 μm effective area between the electrodes (as observed for purely electrochemical cycling[30]). Full-width-at-half-maxima of longitudinal and lateral intensity profiles amount to 20 μm and 4.3 μm, respectively. Presumably, the optical resolution of the 40× objective as well as inhomogeneous transparency of Pt and glass lead to a slightly wider profile than expected. Clearly, ECL emission is confined to the active area of the nanochannel, where reactions (1–4) (Fig. 2b) take place.

The constant ECL intensity along the nanochannel (Fig. 3b, blue curve) indicates that only negligible degradation occurs. If $[Ru(bpy)_3]^+$ or $[Ru(bpy)_3]^{3+}$ would degrade, the intensity would be strongly attenuated in the center of the channel because the chance of encountering contaminants increases quadratically as luminophores diffuse towards the center.

Fig. 4a displays the chronoamperometric currents at both electrodes when stepping between redox cycling and annihilation ECL modes. In redox cycling mode, the oxidation and reduction currents are symmetric and constant. The observed currents of ~0.65 μA are in agreement with an expected analytical estimate[31] of $I_{lim} = \frac{FADc}{h} = 0.58$ μA (F: faraday constant; A: active area of 3 μm by 20 μm; $D = 1 \times 10^{-9}$ m^2 s^{-1} diffusion coefficient, c: 10 mM $[Ru(bpy)_3]^{2+}$ concentration, h: 100 nm channel height).

ECL intensity was measured simultaneously by using a photomultiplier tube (Hamamatsu R4632). The signal was amplified by a Keithley Picoammeter before acquisition with the second input signal of a μAutolab type II potentiostat. Emission was not observed in redox cycling mode (Fig. 4b). Upon switching to annihilation mode, an initial transient current increase can be ascribed to adsorption of analytes onto the electrode surfaces due to the high surface-to-volume ratio of the nanogap devices.[22,29,32] Oxidation and reduction currents are symmetric as expected for reactions (1–4). In annihilation mode, the light intensity (Fig. 4b) exhibits a strong transient behavior before approaching a steady state. Understanding this transient behavior will require further studies, we partially attribute the complex transient to desorption when stepping the potential as well as accumulating $[Ru(bpy)_3]^{3+}$ during redox cycling.

Upon switching from redox cycling to annihilation mode, an expected increase in the current is observed as the diffusive path for cycling molecules halves to 50 nm. Concentration profiles of all $[Ru(bpy)_3]$ species are illustrated in Fig. 5 (COMSOL Multiphysics, see ESI†). Considering the symmetry of the nanofluidic channel and the annihilation reaction (*i.e.*, double cycling redox process), ECL is emitted in the middle of the

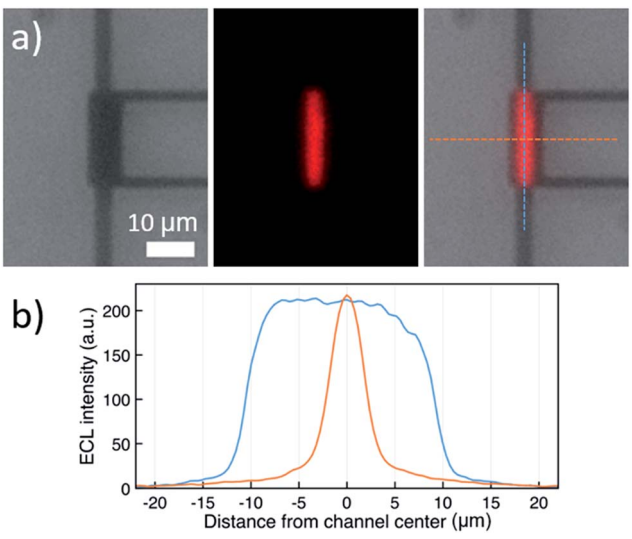

Fig. 3 (a) From left to right: bright-field micrograph of the nanochannel, ECL emission recorded in the dark, and overlay of both images (dashed lines: direction of profiles in (b)). (b) ECL intensity profiles along (blue) and across (orange) the center of the channel, using a solution of 10 mM $Ru(bpy)_3(PF_6)_2$ and 0.1 M $TBAPF_6$ in acetonitrile. The top electrode was biased at 2 V, the bottom electrode at −1.5 V *vs.* Ag.

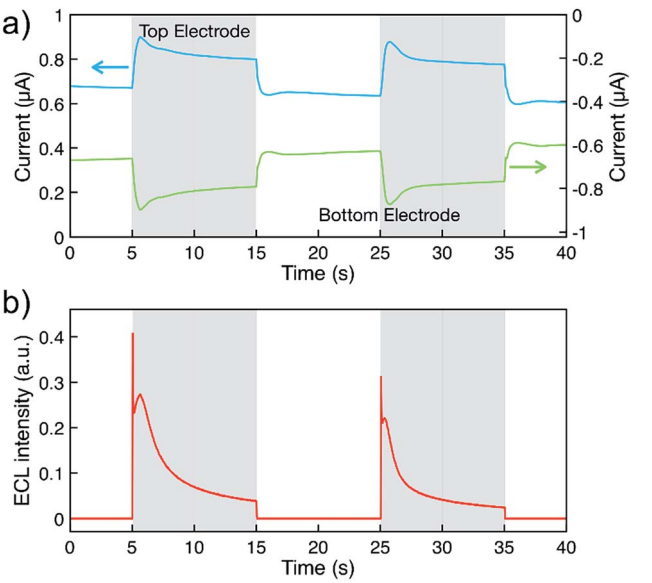

Fig. 4 (a) Measured chronoamperometric currents at the top (blue) and bottom (green) electrodes, and (b) corresponding ECL intensity. The top electrode was maintained at 2.3 V while the bottom electrode was pulsed between 0 V and −1.5 V *vs.* Ag, highlighted in white (redox cycling mode) and grey (annihilation ECL mode), respectively. Solution consisted of 10 mM $Ru(bpy)_3(PF_6)_2$ and 0.1 M $TBAPF_6$ in acetonitrile.

nanogap where both $[Ru(bpy)_3]^{3+}$ and $[Ru(bpy)_3]^{+}$ react to form $[Ru(bpy)_3]^{2+}$*, assuming similar diffusion coefficients for $[Ru(bpy)_3]^{3+}$ and $[Ru(bpy)_3]^{+}$. The ECL emission should occur in the vertical symmetry plane of the device and be confined to the electroactive area of the nanochannel (see Fig. 5d). However, it is not possible to resolve this with optical microscopy due do the nanometric dimension of the inter-electrode gap.

The simulated diffusive fluxes (*i.e.*, slopes of concentration profiles) at electrode surfaces double when switching from redox cycling to annihilation. However, a ratio of only 1.2 for the steady-state redox cycling and annihilation currents is observed (Fig. 4a). Understanding this low ratio requires further studies. As origin we rule out degradation (see above) and a limited annihilation rate (as a two-electron electrode reaction of $[Ru(bpy)_3]^{+}$ and $[Ru(bpy)_3]^{3+}$ would exactly compensate for every annihilation not taking place[18,33,34]). Furthermore, any influences on the currents by unequal diffusivities as well as by adsorption are balanced by coupling to the bulk reservoir.[29,31] We speculate that more complex concentration profiles are caused by contribution of electrical migration (at an overall potential drop of 3.5 V over 100 nm).

Classically, annihilation ECL experiments are performed using highly inert conditions (*vide supra*).[15,18,20] In the present work, we imaged an intense ECL signal under ambient conditions using platinum electrodes. In the nanochannel, neither strong degradation of $[Ru(bpy)_3]^{+}$ nor greatly reduced annihilation occurs (previously reduction of the annihilation rate from $>10^7$ M^{-1} s^{-1} to $\sim10^3$ M^{-1} s^{-1} was observed under ambient conditions[18,35]). Negligible degradation is caused by the short diffusive path, which greatly reduces the chance to encounter contaminants such as dioxygen, and/or by depletion of contaminants in the nanochannel by electrochemical deactivation at the electrodes (in the ESI† we further explore the effect of channel height, lifetime of the excited state and possible degradation on concentration profile by finite element calculations).

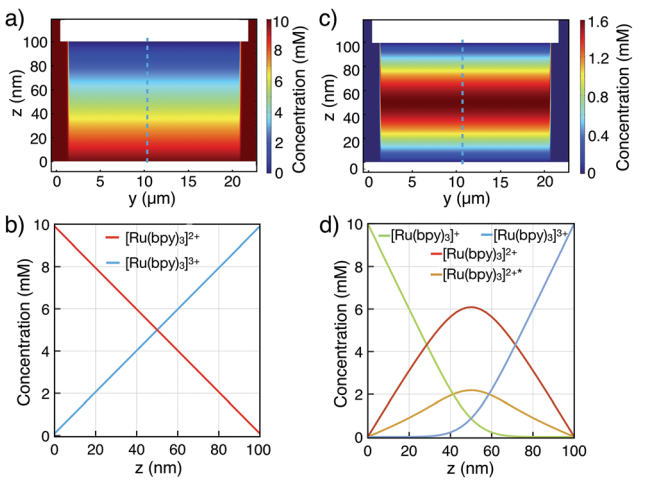

Fig. 5 Finite element simulations of concentration profiles for a 10 mM $[Ru(bpy)_3]^{2+}$ bulk concentration in the nanochannel. Two-dimensional $[Ru(bpy)_3]^{2+}$ profiles in (a) redox cycling mode, and (c) annihilation mode. (b and d) Corresponding cross-sectional profiles in the channel center (indicated by the dashed line in both modes, respectively).

Conclusions

ECL-emission was investigated in transparent nanofluidic devices for the first time. Light emission was shown to occur through an annihilation reaction pathway when both electrodes were biased at appropriate potentials. Light emission is enhanced in two ways: first, the close vicinity of the two electrodes leads to efficient annihilation reactions due to very fast diffusion. Second, stable light emission is achieved as the very short diffusive distances protect from degradation by contaminants, and our results indicate that measurements in nanodevices are possible under ambient conditions, which cannot be achieved using classical setups. Microfabricated nanodevices combine the properties of exact control of an inter-electrode distance, a highly reproducible device geometry and strong confinement of analytes in the channel volume. Therefore, we believe that nanogap transducers are powerful tools for investigating pathways in ECL and also to exploit their unique nanometric properties to develop multicolor ECL emission systems.

Conflicts of interest

There are no conflicts to declare.

Acknowledgements

We thank the Agence Nationale de la Recherche (MOLY, ANR-15-CE19-0005-01; NEOCLASSIC ANR-15-CE09-0015-03). We thank Dr Giovanni Valenti (University of Bologna) for helpful discussions.

References

1 A. Bard, *Electrogenerated chemiluminescence*, Marcel Dekker, New York, 2004.
2 A. J. Wilson, K. Marchuk and K. A. Willets, *Nano Lett.*, 2015, **15**, 6110–6115.
3 J. E. Dick, C. Renault, B. K. Kim and A. J. Bard, *Angew. Chem., Int. Ed.*, 2014, **53**, 11859–11862.
4 G. Valenti, S. Scarabino, B. Goudeau, A. Lesch, M. Jović, E. Villani, M. Sentic, S. Rapino, S. Arbault, F. Paolucci and N. Sojic, *J. Am. Chem. Soc.*, 2017, **139**, 16830–16837.
5 L. Hu and G. Xu, *Chem. Soc. Rev.*, 2010, **39**, 3275–3304.
6 B. A. Gorman, P. S. Francis and N. W. Barnett, *Analyst*, 2006, **131**, 616–639.
7 X. B. Yin, S. Dong and E. Wang, *TrAC, Trends Anal. Chem.*, 2004, **23**, 432–441.
8 R. J. Forster, P. Bertoncello and T. E. Keyes, *Annu. Rev. Anal. Chem.*, 2009, **2**, 359–385.
9 R. Breslow, R. Hill and E. Wasserman, *J. Am. Chem. Soc.*, 1964, **83**, 5350–5351.
10 K. S. V. Santhanam and A. J. Bard, *J. Am. Chem. Soc.*, 1965, **87**, 139–140.

11 F. F. Fan, in *Electrogenerated Chemiluminescence*, ed. A. J. Bard, CRC Press, New York, 1st edn, 2004, pp. 23–99.
12 J. T. Maloy, K. B. Prater and A. J. Bard, *J. Am. Chem. Soc.*, 1971, **93**, 5959–5968.
13 G. H. Brilmyer and A. J. Bard, *J. Electrochem. Soc.*, 1980, **127**, 104–110.
14 J. E. Bartelt, S. M. Drew and R. M. Wightman, *J. Electrochem. Soc.*, 1992, **139**, 70–74.
15 C. Amatore, C. Pebay, L. Servant, N. Sojic, S. Szunerits and L. Thouin, *ChemPhysChem*, 2006, **7**, 1322–1327.
16 G. C. Fiaccabrino, M. Koudelka-Hep, Y. T. Hsueh, S. D. Collins and R. L. Smith, *Anal. Chem.*, 1998, **70**, 4157–4161.
17 F.-R. F. Fan, D. Cliffel and A. J. Bard, *Anal. Chem.*, 1998, **70**, 2941–2948.
18 J. Rodríguez-López, M. Shen, A. B. Nepomnyashchii and A. J. Bard, *J. Am. Chem. Soc.*, 2012, **134**, 9240–9250.
19 M. Shen, N. Arroyo-Currás and A. J. Bard, *Anal. Chem.*, 2011, **83**, 9082–9085.
20 A. Kapturkiewicz and G. Angulo, *Dalton Trans.*, 2003, 3907–3913.
21 M. A. G. Zevenbergen, D. Krapf, M. R. Zuiddam and S. G. Lemay, *Nano Lett.*, 2007, **7**, 384–388.
22 D. Mampallil, K. Mathwig, S. Kang and S. G. Lemay, *J. Phys. Chem. Lett.*, 2014, **5**, 636–640.
23 Q. Chen, K. McKelvey, M. A. Edwards and H. S. White, *J. Phys. Chem. C*, 2016, **120**, 17251–17260.
24 C. Ma, W. Xu, W. R. A. Wichert and P. W. Bohn, *ACS Nano*, 2016, **10**, 3658–3664.
25 L. Rassaei, K. Mathwig, S. Kang, H. A. Heering and S. G. Lemay, *ACS Nano*, 2014, **8**, 8278–8284.
26 S. Kang, A. F. Nieuwenhuis, K. Mathwig, D. Mampallil, Z. Kostiuchenko and S. G. Lemay, *Faraday Discuss.*, 2016, **193**, 41–50.
27 D. Han, G. M. Crouch, K. Fu, L. P. Zaino III and P. W. Bohn, *Chem. Sci.*, 2017, **8**, 5345–5355.
28 K. Mathwig and S. G. Lemay, *Micromachines*, 2013, **4**, 138–148.
29 S. Kang, K. Mathwig and S. G. Lemay, *Lab Chip*, 2012, **12**, 1262–1267.
30 S. Kang, A. F. Nieuwenhuis, K. Mathwig, D. Mampallil and S. G. Lemay, *ACS Nano*, 2013, **7**, 10931–10937.
31 D. Mampallil, K. Mathwig, S. Kang and S. G. Lemay, *Anal. Chem.*, 2013, **85**, 6053–6058.
32 E. Kätelhön, K. J. Krause, K. Mathwig, S. G. Lemay and B. Wolfrum, *ACS Nano*, 2014, **8**, 4924–4930.
33 Q. Wang, J. Rodríguez-López and A. J. Bard, *ChemPhysChem*, 2010, **11**, 2969–2978.
34 C. Amatore, F. BonhSomme, J. L. Bruneel, L. Servant and L. Thouin, *J. Electroanal. Chem.*, 2000, **484**, 1–17.
35 M. M. Collinson, R. M. Wightman and P. Pastore, *J. Phys. Chem.*, 1994, **98**, 11942–11947.

Supporting Information for:

Enhanced Annihilation Electrochemiluminescence by Nano-fluidic Confinement

Hanan Al-Kutubi,[§] Silvia Voci,[#] Liza Rassaei,[‡,¶] Neso Sojic,[,#] and Klaus Mathwig*[,§]*

§ University of Groningen, Groningen Research Institute of Pharmacy, Pharmaceutical Analysis, P.O. Box 196, 9700 AD Groningen, The Netherlands

Univ. Bordeaux, CNRS UMR 5255, Bordeaux INP, Site ENSCBP, 33607 Pessac, France

‡ Rotterdam School of Management, Erasmus University, Burgemeester Oudlaan 50, 3062 PA Rotterdam, The Netherlands

¶ Delft University of Technology, Van der Maasweg 9, 2629 HZ Delft, The Netherlands

Email: neso.sojic@enscbp.fr; k.h.mathwig@rug.nl

Contents

1. Chemical reagents

Tris(2,2'-bipyridine)ruthenium(II) hexafluorophosphate ($Ru(bpy)_3(PF_6)_2$), sulfuric acid and the supporting electrolyte tetrabutylammonium hexafluorophosphate ($TBAPF_6$) were purchased from Sigma-Aldrich, chromium etchant (Selectipur) from BASF. All solutions were prepared using Milli-Q water (resistivity = 18 MΩ cm) or HPLC-grade acetonitrile (Sigma-Aldrich).

2. Device Fabrication

Figure S1 shows the fabrication steps of electrochemical nanofluidic devices. See ref. 1 for further details of the process. Process parameters were optimized to accommodate the properties of a transparent borosilicate substrate in contrast to substrates of opaque oxidized Si wafers used previously.

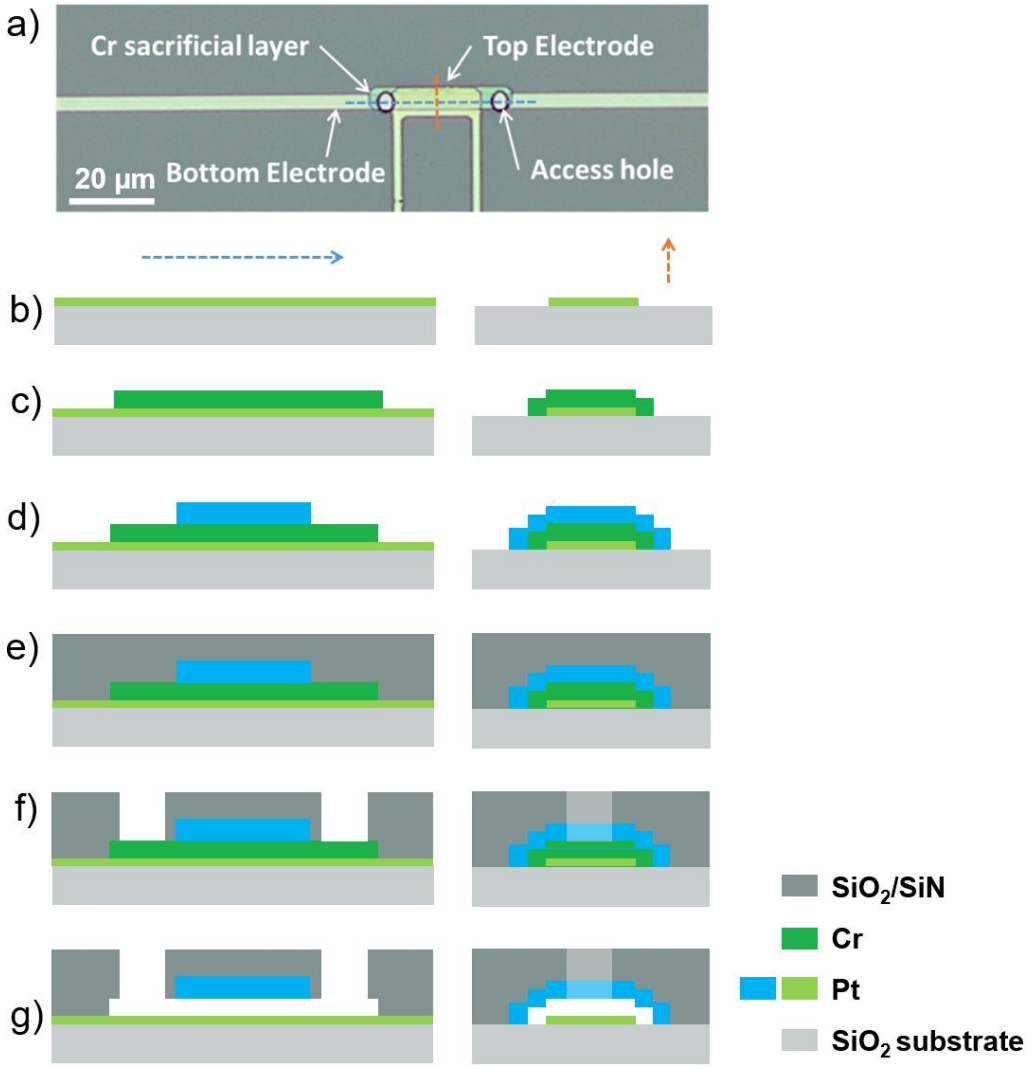

Figure S1: *Microfabrication steps of transparent nanofluidic electrochemical transducers. a) Top-view micrograph of a device, indicating the longitudinal (blue dashed line) and lateral (orange) cross section in the schematic below. b) Patterning of a 20-nm-thick Pt layer by photolithography, metal evaporation and a lift-off process. A 10-cm-wide and 700-µm-thick borosilicate wafer substrate was used. c) Photolithography, metal evaporation, and lift-off to structure the Cr layer defining the nanochannel volume. d) Photolithography, Pt evaporation and lift-off to define the top electrode. e) PECVD deposition of a SiO_2/SiN/SiO_2 passivation layer. f) photolithography and reactive ion etching of access holes through the passivation layer using the resist as mask. g) The wafer is diced into individual chips. Directly before and experiment, the Cr layer is removed and the nanochannel is formed using a selective wet chemical Cr etch.*

3. Background measurement with one electrode

As a control, an experiment was performed where the bottom electrode of a nanofluidic device was disconnected (i.e., kept at a floating potential) while the top electrode was pulsed between 0 V and 2.0 V vs. Ag wire. The chronoamperometric current and light intensity response measured with a photomultiplier tube are both shown in Figure S2.

While pulsing a single electrode, the change in detected light intensity is negligible compare to the background intensity. This observation demonstrates that two independently biased electrodes (at constant) potentials are necessary for the generation of electrochemiluminescence; indicating that light generation takes place according to the annihilation pathway shown in reactions (1-4) in the main text.

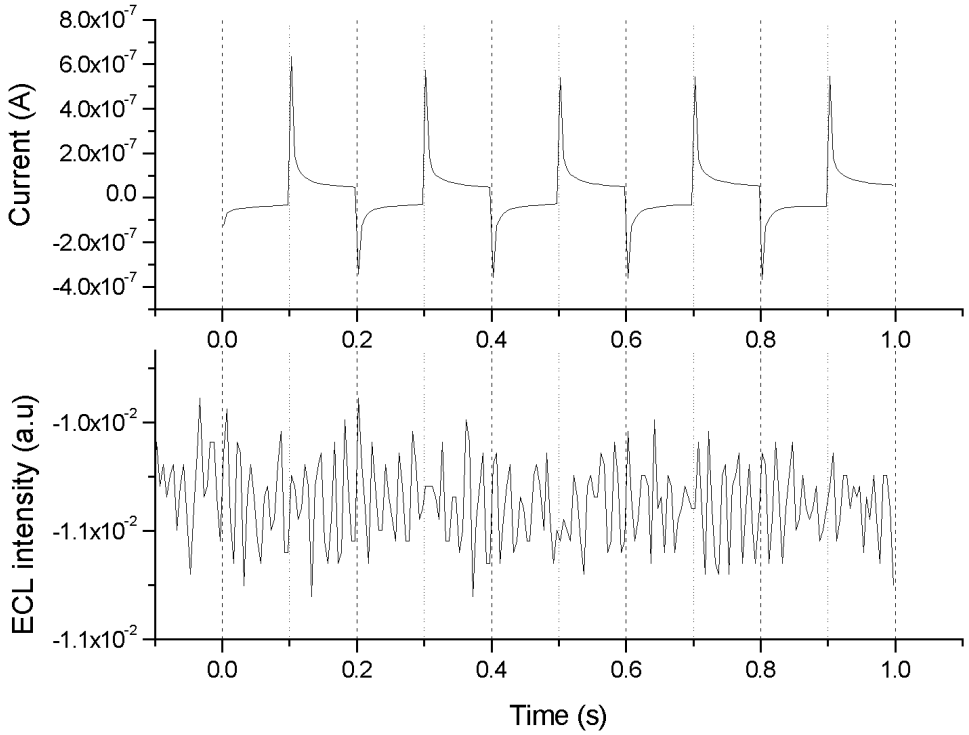

***Figure S2**: Measured chronoamperometric currents (top) and corresponding light intensity recorded with a PMT (bottom). A potential alternating between 0 V and 2.0 V vs. Ag was applied to the top electrode of a nanogap device while the bottom electrode was kept floating. A solution of 10 mM $Ru(bpy)_3(PF_6)_2$ and 0.1 M $TBAPF_6$ in acetonitrile was used.*

4. Finite element modeling

Two-dimensional finite element modeling **(**COMSOL Multiphysics 5.2a) was employed to determine steady-state concentration profiles of the different $Ru(bpy)_3$ ion species. The geometry consists of the channel itself with a length of overall 20 µm and a height of 100 nm. 2 µm wide access holes at both ends of the channel couple the nanochannel to a larger reservoir. The top electrode is defined as a 20-µm-long segment in the center of the upper boundary of the nanochannel, while the bottom electrode covers the entire channel floor segment.

For the simulation, we considered diffusion as the only mass transport mechanism (i.e., no convection, and no electrical migration at a high concentration of background electrolyte) described by Fick's second law:[2]

$$\frac{\partial c_j}{\partial t} = D\nabla^2 c_j$$

Here, $c_{j=1,2,3,4}$ denotes the concentrations of the four compounds $[Ru(bpy)_3]^+$, $[Ru(bpy)_3]^{2+}$, $[Ru(bpy)_3]^{3+}$, and $[Ru(bpy)_3]^{2+}$*, respectively. We assumed an equal diffusion coefficient of $D = 1\times10^{-9}$ m^{2}s^{-1} for all species.[3] A starting concentration of 10 mM $[Ru(bpy)_3]^{2+}$ was chosen in the entire simulation geometry, and a reservoir boundary was set to a constant concentration of also 10 mM $[Ru(bpy)_3]^{2+}$ (boundary and starting conditions of 0 M $[Ru(bpy)_3]^+$, 0 M $[Ru(bpy)_3]^{3+}$, and 0 mM $[Ru(bpy)_3]^{2+}$*).

To determine concentration profiles in annihilation mode we simulated four reactions as shown in the main text:

$$[Ru(bpy)_3]^{2+} + e^- \rightarrow [Ru(bpy)_3]^+ \quad (1)$$

$$[Ru(bpy)_3]^{2+} - e^- \rightarrow [Ru(bpy)_3]^{3+} \quad (2)$$

$$[Ru(bpy)_3]^+ + [Ru(bpy)_3]^{3+} \xrightarrow{k_{ann}} [Ru(bpy)_3]^{2+} + [Ru(bpy)_3]^{2+*} \quad (3)$$

$$[Ru(bpy)_3]^{2+*} \xrightarrow{k_4} [Ru(bpy)_3]^{2+} + h\nu \quad (4)$$

In addition, we considered the possibility of 2-electron reactions at the electrodes (which occur when $[Ru(bpy)_3]^+$ or $[Ru(bpy)_3]^{3+}$ crosses the nanochannel without participating in annihilation):

$$[Ru(bpy)_3]^{3+} + 2e^- \rightarrow [Ru(bpy)_3]^+ \quad (5)$$

$$[Ru(bpy)_3]^+ - 2e^- \rightarrow [Ru(bpy)_3]^{3+}. \quad (6)$$

At the electrode surfaces, we implemented a Butler-Volmer formalism[4] calculating normal molar influxes N_j at the positively biased top electrode (species 1, 2 and 4 are consumed, and an influx N_3 of species 3 is generated):

$$N_1 = k_{13,f}c_3 - k_{13,b}c_1 \quad (7)$$

$$N_2 = k_{23,f}c_3 - k_{23,b}c_2 \quad (8)$$

$$N_3 = k_{23,b}c_2 - k_{23,f}c_3 + k_{23,b}c_4 + k_{13,b}c_1 - k_{13,f}c_3 \quad (9)$$

$$N_4 = -k_{23,b}c_4, \quad (10)$$

and at the bottom electrode (negative bias, normal influx N_1 of $[Ru(bpy)_3]^+$, consumption of all other ions):

$$N_1 = k_{21,b}c_2 - k_{21,f}c_1 + k_{21,b}c_4 + k_{31,b}c_3 - k_{31,f}c_1 \quad (11)$$

$$N_2 = k_{21,f}c_1 - k_{21,b}c_2 \quad (12)$$

$$N_3 = k_{31,f}c_1 - k_{31,b}c_3 \quad (13)$$

$$N_4 = -k_{21,b}c_4. \quad (14)$$

Here, the forward and backward rate constants are defined as:

$$k_{13,f} = k_{23,f} = k_0 \exp\left[\frac{-\alpha F(E_{\text{top}} - E_{h(\text{ox})})}{RT}\right] \quad (15)$$

$$k_{13,b} = k_{23,b} = k_0 \exp\left[\frac{(1-\alpha) F(E_{\text{top}} - E_{h(\text{ox})}}{RT}\right] \quad (16)$$

$$k_{31,f} = k_{32,f} = k_0 \exp\left[\frac{-\alpha F(E_{\text{bot}} - E_{h(\text{red})})}{RT}\right] \quad (17)$$

$$k_{31,b} = k_{32,b} = k_0 \exp\left[\frac{(1-\alpha) F(E_{\text{bot}} - E_{h(\text{red})}}{RT}\right]. \quad (18)$$

F, R, and T are the Faraday constant, gas constant and temperature, respectively, $\alpha = 0.5$ the charge transfer coefficient. A high standard rate constant of $k_0 = 0.01$ m s^{-1} was chosen for all electrode reactions. For the difference of the applied potentials (at the top and bottom electrode, respectively) and the formal respective potentials for oxidation/reduction we chose the same high overpotentials as in the experiment ($E_{\text{top}} = 2$ V, $E_{\text{red}} = -1.5$ V, $E_{h(\text{ox})} = 1.35$ V, $E_{h(\text{red})} = -1.27$ V).

In the bulk of the nanochannel, we implemented eq. (3,4) as reactions R_j (in M s^{-1}) of the generation and consumption of species with concentrations c_j:

$$R_1 = -k_{\text{ann}} c_1 c_3 \quad (19)$$

$$R_2 = k_{\text{ann}} c_1 c_3 + k_4 c_4 \quad (20)$$

$$R_3 = -k_{\text{ann}} c_1 c_3 \quad (21)$$

$$R_4 = k_{\text{ann}} c_1 c_3 - k_4 c_4. \quad (22)$$

For the concentration profiles shown in Figure 5c,d in the main text we considered a fast annihilation rate of $k_{\text{ann}} = 10^{10}$ M^{-1} s^{-1} as well as a lifetime of the excited state $[Ru(bpy)_3]^{3+}$* of 1 µs ($k_4 = 10^6$ s^{-1}). Light generation hν was not considered explicitly.

Due to the fast efficient annihilation with the rate k_{ann} the vast majority of generated species $[Ru(bpy)_3]^{+}$ and $[Ru(bpy)_3]^{3+}$ undergo annihilation in the bulk nanochannel, reducing their concentrations to almost 0 mM at the top and bottom electrode, respectively. Therefore, the current obtained is almost exclusively due to the 1-electron processes (1,2) taking place, dominating 2-electron processes (5,6).

The sum of the concentration of $[Ru(bpy)_3]^{2+}$ and $[Ru(bpy)_3]^{2+}$* in the center of the channel (z=50 nm) amounts to approximately 8 mM. An infinitely fast annihilation would lead to a concentration of 10 mM.

The concentration of $[Ru(bpy)_3]^{2+}$* and hence the ratio of concentrations of $[Ru(bpy)_3]^{2+}$* to $[Ru(bpy)_3]^{2+}$ is determined by k_4 (4), i.e., by the lifetime of the excited state. For the chosen k_4-value, a ratio of about 1:3 was obtained. The $[Ru(bpy)_3]^{2+}$* concentration profile shows that light is emitted predominantly from the vertical symmetry plane of the nanochannel.

To simulate concentration profiles in redox cycling mode (Fig. 5a,b in the main text), we considered oxidation at the top electrode:

$$N_2 = k_{23,f} c_3 - k_{23,b} c_2 \quad (22)$$

$$N_3 = k_{23,b} c_2 - k_{23,f} c_3, \quad (23)$$

and reduction at the bottom electrode:

$$N_2 = k_{23,f} c_3 - k_{23,b} c_2 \quad (24)$$

$$N_3 = k_{32,f} c_2 - k_{32,b} c_3. \quad (25)$$

At the chosen high overpotentials, linear concentration profiles are established across the nanochannel as expected.[5] (Only the standard potential $E_{h(\mathrm{ox})}$ and a potential of the bottom electrode of $E_{\mathrm{red}} = 0$ V were used for simulating the redox cycling mode).

5. Numerical concentration profiles

5.1 Variation of exited-state lifetime

To explore the effect of the lifetime of the excited $[Ru(bpy)_3]^{2+*}$ luminophore state on concentration profiles in the nanochannel, we varied it in a two-dimensional COMSOL simulation from 10 µs ($k_4 = 10^5$ s^{-1}) to 1 µs ($k_4 = 10^6$ s^{-1} as shown in Fig. 5 in the main text) to 0.1 µs ($k_4 = 10^7$ s^{-1}). Simulated concentration profiles in annihilation mode are shown in Figure S3.

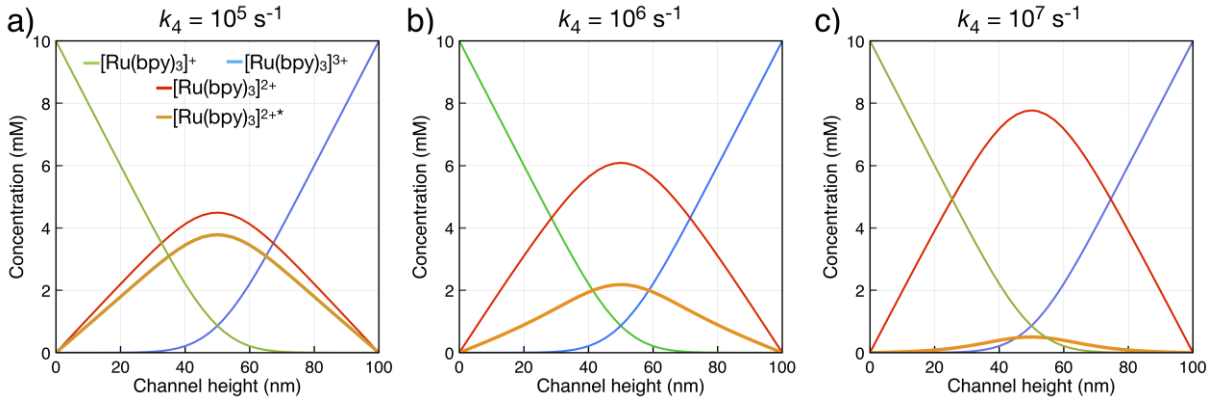

Figure S3: *Finite element simulation of concentration profiles of a 10 mM $[Ru(bpy)_3]^{2+}$ bulk concentration in the nanochannel. Cross-sectional profiles of a two-dimensional numerical geometry are shown. The lifetime of the excited state is a) 10 µs, b) 1 µs, and c) 0.1 µs.*

For a lifetime longer than the diffusion time across (half) the channel (see Fig. S3a), a large flux of excited-state ions to the electrodes is observed (evident by the steep slope of the orange graph at z = 0 nm and z = 100 nm in Fig. S3a). In this case, a majority of $[Ru(bpy)_3]^{2+*}$ ions reacts at the electrodes before emitting a photon.

For very short-lived excited luminophore states (see Fig. S3c), their flux towards the electrode is reduced to virtually 0, and all of them relax to the ground state.

In the likely experimental case of a $[Ru(bpy)_3]^{2+*}$ lifetime of 1 µs (see Fig. S3b and Fig. 5 in the main text), most luminophores will relax to the ground state before reaching an electrode by diffusion (the concentration of $[Ru(bpy)_3]^{2+*}$ is less than half of the $[Ru(bpy)_3]^{2+}$ concentration at any position across the nanochannel). Nonetheless, a considerable amount of $[Ru(bpy)_3]^{2+*}$ is oxidized or reduced before the end of their lifetime and will not contribute to ECL emission.

5.2 Variation of nanochannel height

We changed the height of the nanochannel in the numerical simulation to elucidate its effect on concentration profiles and expected ECL intensity as shown in Figure S4 for channel heights of 50 nm, 100 nm, 200 nm, and 500 nm.

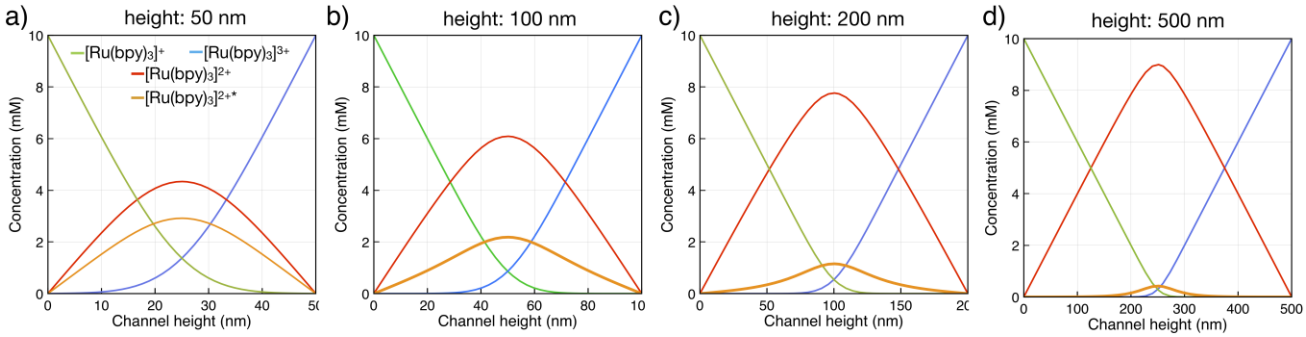

Figure S4: *Finite element simulation of concentration profiles of a 10 mM $[Ru(bpy)_3]^{2+}$ bulk concentration for various channel heights of a) 50 nm, b) 100 nm, c) 200 nm, and d) 500 nm. The lifetime of the $[Ru(bpy)_3]^{2+}$* state was set at 1 µs ($k_4 = 10^6\ s^{-1}$). (Panel (b) is identical to Fig. 5d in the main text.)*

The effect of a changed height (and, thus, different diffusion times across the channel) on the profiles is comparable to the effect of varied lifetimes: For diffusion times longer than excited-state lifetimes, a greater number of luminophores emit light before reaching an electrode surface (e.g., at heights of 200 nm and 500 nm).

With an increased channel height, the diffusion time also increases as compared to the high annihilation rate of $k_{ann} = 10^{10}\ M^{-1}\ s^{-1}$. Therefore, $[Ru(bpy)_3]^{2+}$ profiles shift from a "parabolic" to a sharp "triangular" shape.

We predict that changing the nanochannel height will have various effects on the intensity of light emission: Overall, emission will increase *linearly* with decreased height. (Intensity would increase *quadratically* as diffusion times are reduced quadratically. However, the channel volume, and, thus, the number of molecules participating in ECL, is also reduced linearly for shallower channels). In addition, if the channel is very shallow, light emission will decrease as oxidation/reduction starts to dominate relaxation and photon emission. We estimate that our experimental nanochannel height of 100 nm could correspond to a value close to the maximum of light emission for a $[Ru(bpy)_3]^{2+}$* lifetime of 1 µs.

5.3 Degradation of $[Ru(bpy)_3]^+$

We numerically evaluate a possible effect of degradation of $[Ru(bpy)_3]^{3+}$ or $[Ru(bpy)_3]^+$ ions by contaminants on profiles of concentration and light emission. An exemplary degradation reaction is

$$[Ru(bpy)_3]^+ + O_2^- \xrightarrow{k_{deg}} P_1. \qquad (26)$$

Oxidized $[Ru(bpy)_3]^+$ ions react to a product P_1, which does not participate in ECL annihilation anymore. To simulate such a reaction, we added a degradation term to equation (19), it is replaced by

$$R_1 = -k_{ann} c_1 c_3 - k_{deg} c_1. \qquad (27)$$

This means, the concentration c_1 of $[Ru(bpy)_3]^+$ is continously reduced in the bulk of the nanochannel (and reservoir) at a rate k_{deg}. The expected effect on concentration profiles *along* the nanochannel is shown in Figure S5.

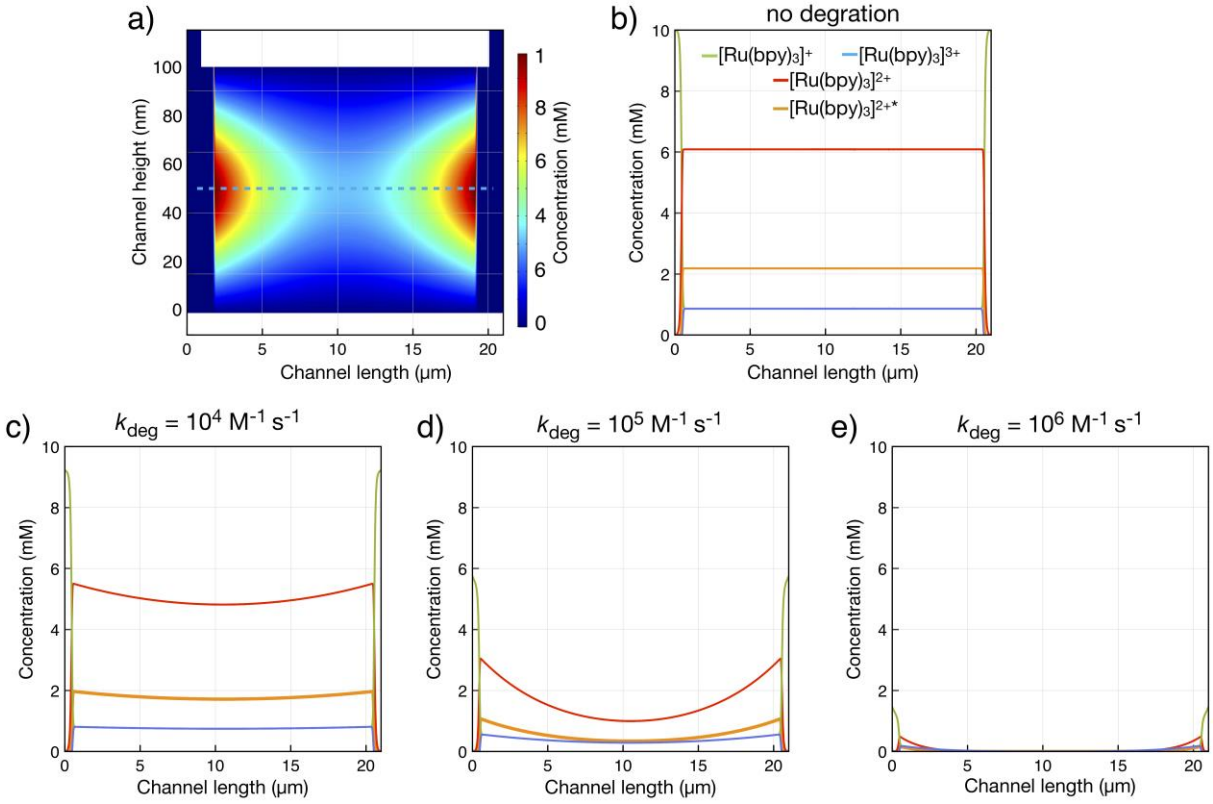

Figure S5: *Finite element simulation of concentration profiles of a 10 mM $[Ru(bpy)_3]^{2+}$ bulk concentration for varied rates of $[Ru(bpy)_3]^+$ degradation k_{deg} (and $k_4 = 10^6\ s^{-1}$; $k_{ann} = 10^{10}\ M^{-1}\ s^{-1}$). a) Two-dimensional $[Ru(bpy)_3]^{+*}$ profile for $k_{deg} = 10^5\ M^{-1}\ s^{-1}$. (b-e) Corresponding profiles* along *the channel (dashed line in a) for: b) no degradation c) $k_{deg} = 10^4\ M^{-1}\ s^{-1}$, c) $k_{deg} = 10^5\ M^{-1}\ s^{-1}$ a (orang curve corresponds to two-dimensional profile in a) and, e) $k_{deg} = 10^6\ M^{-1}\ s^{-1}$.*

The concentration of $[Ru(bpy)_3]^{+*}$ *along* the channel center is proportional to the intensity of emitted light. By comparison to the experimentally determined light emission profile (see Figure 3b in the main text), which shows homogenous intensity along the channel, we estimate that potential degradation by contaminants is limited to a rate lower than about 10^4 M^{-1} s^{-1}.

References

1 S. Kang, K. Mathwig and S. G. Lemay, *Lab Chip*, 2012, **12**, 1262–7.

2 H. R. Zafarani, K. Mathwig, E. J. R. Sudhölter and L. Rassaei, *J. Electroanal. Chem.*, 2016, **760**, 42–47.

3 C. Amatore, B. Fosset, K. M. Mannes and M. R. Wightman, *Anal. Chem.*, 1993, **65**, 2311–2316.

4 G. Valenti, S. Scarabino, B. Goudeau, A. Lesch, M. Jović, E. Villani, M. Sentic, S. Rapino, S. Arbault, F. Paolucci and N. Sojic, *J. Am. Chem. Soc.*, 2017, **139**, 16830–16837.

5 K. Mathwig and S. G. Lemay, *Electrochim. Acta*, 2013, **112**, 943–949.